Oxford Open Materials Science, 2025, **5(1)**, itaf005
https://doi.org/10.1093/oxfmat/itaf005
Advance Access Publication Date: 23 April 2025
Research article

Polycrystalline $BiVO_4$ visible-light photocatalytic activity: Rietveld refinement, microstructural, vibrational, and photocatalytic properties

Safia Lotfi[1], Mohamed El Ouardi[1,2], Madjid Arab[2], Abderrazzak Assani[1], Amal BaQais[3], Henrik Haspel[4,5], Zoltán Kónya[4,5], Hassan Ait Ahsaine[1,*]

[1]Laboratoire de Chimie Appliquée des Matériaux, Centre des Sciences des Matériaux, Faculty of Sciences, Mohammed V University in Rabat, Morocco
[2]AMU, CNRS, IM2NP, Université de Toulon, CS 60584, Toulon Cedex 9, France
[3]Department of Chemistry, College of Science, Princess Nourah Bint Abdulrahman University, P. O. Box 84428, Riyadh 11671, Saudi Arabia
[4]HUN-REN-SZTE Reaction Kinetics and Surface Chemistry Research Group, Rerrich Béla tér 1, H-6720 Szeged, Hungary
[5]Department of Applied and Environmental Chemistry, University of Szeged, Rerrich Béla tér 1, H-6720 Szeged, Hungary

*Corresponding author. Laboratoire de Chimie Appliquée des Matériaux, Centre des Sciences des Matériaux, Faculty of Sciences in Rabat, Mohammed V University in Rabat, BP 1014 RP, RABAT, Morocco. Email: h.aitahsaine@um5r.ac.ma

Abstract

Herein, we have successfully synthesized $BiVO_4$ photocatalysts via a simple chemical precipitation method followed by heat treatment at 400°C, 500°C, and 600°C. The samples were characterized by XRD combined with Rietveld refinement, Raman spectroscopy, SEM, and UV- vis DRS. XRD results showed that we obtained monoclinic scheelite phase (m-s $BiVO_4$) with I112/b space group. The visible–light photocatalytic activities of $BiVO_4$ -400°C, 500°C, and 600°C for organic dye degradation (MB: methylene blue; MO: and methyl orange) were investigated, and the BiVO4 400°C showed the highest activity in the photodegradation of MB (95%) and MO (80%) after 150 min of visible illumination. The photocatalytic degradation mechanism was proposed based on radical trapping measurements and Mott–Schottky analysis.

Keywords: bismuth vanadate; photocatalysis; visible-light; dye degradation, active species; photocatalytic activity

Introduction

Recent decades have seen rapid growth of urbanization of the global population and industrial development that led to water pollution and scarcity on every continent [1, 2]. This phenomenon is a consequence of the direct discharge of domestic and industrial wastes, including heavy metals, residual non-biodegradable dyes, pesticides, and bacteria [3–8]. These dangerous substances have harmful impacts on the environment and the human health, while it was also reported that 80% of diseases and 50% of deaths can be linked to wastewater [9]. Therefore, various treatment technologies were utilized [10, 11], such as coagulation [12], flocculation [13], ion exchange [14], chemical precipitation [15], sedimentation [16], and chlorination [17]. Despite having been used for decades, the above methods proved to be expensive and partly ineffective as they cannot completely remove pollutants [5, 18, 19]. As an alternative approach, semiconductor photocatalysis has attracted the attention of researchers in the past decades [20]. This process is a promising environmental-friendly technology, which utilizes the sunlight as a renewable source for the generation of electron-hole pairs in semiconducting catalyst particles. The excited charge carriers lead to the production of reactive oxygen species ($O_2^{\bullet -}$ and $^{\bullet}OH$), which, in turn, participate in the chemical degradation of pollutants until their mineralization to CO_2 and H_2O [3, 5, 21–25]. In the past decades, titanium dioxide (TiO_2) was commonly used as photocatalyst for the degradation of organic contaminants due to its high photocatalytic activity, robust chemical stability, wide commercial availability, affordability, and non-toxic nature [5, 26–28]. However, the use of TiO_2 was limited because of its wide bandgap of 3.2 eV, which makes it suitable only for the UV region [2, 29]. To overcome this, non-titania-based narrow bandgap semiconductors were developed with and an effective visible light response [30–32], like $FeVO_4$ [33], Bi_2WO_6 [34, 35], Bi_2O_3 [36], $BiVO_4$ [37], g-C_3N_4 [38], $LaVO_4$ [39], $CeVO_4$ [40], and YVO_4 [41]. Bismuth-based oxides are promising candidates for photocatalytically degrading waste pollutants due to their suitable band gap for visible light absorption [42], along with their low toxicity and high electric conductivity [43]. Taking Bi_2O_3 as an example, it has recently attracted more attention as a photocatalyst for water purification due to its optical properties in the visible region with a narrow band gap of ∼2.8 eV [44]. Unfortunately, its high electron-hole pair recombination rate limits the solar energy utilization, and thus, its photocatalytic activity [45]. Also, its photoinduced dissolution leads to a significant loss of bismuth, which reduces the pollutant degradation efficiency during Bi2O3 reuse as released Bi3+ will be one of the causes of secondary pollution [46]. Bi2O3 presents five

Received: 20 October 2024. **Revised:** 08 February 2025. **Accepted:** 11 March 2025

polymorphic crystal forms: two of them are stable electric conductors (α at low and δ at high temperature), while others are metastable (β, γ, and ω Bi2O3) [45]. Phase transitions are always associated with marked changes in the properties and stability of material, which can be undesirable in applications [47]. Large particles can be formed in the resulting phase having low surface area and reducing the photocatalytic activity of the material [48]. A further material that has attracted attention is graphitic carbonitride (g-C3N4), a promising and sustainable photocatalyst for environmental remediation [38]. However, despite of its beneficial properties, it has a number of limitations just like Bi2O3, such as low surface area, a ~2.7 eV band gap energy, poor absorption in the visible region, and high electron-hole recombination. All these factors reduce photoactivity under visible light irradiation [49, 50]. Among these photocatalysts, bismuth vanadate ($BiVO_4$) has been extensively studied in organic pollutant photodegradation under visible light illumination, as its narrow band gap, non-toxicity, excellent dispersibility, chemical stability, and high-performance make it an ideal candidate [5, 51–53]. Although $BiVO_4$ has three crystal phases: (i) tetragonal scheelite, (ii) tetragonal zircon, and (iii) monoclinic scheelite [54], only the monoclinic scheelite $BiVO_4$ (m–s) possess excellent photocatalytic activity due to the combination of its narrow band gap (2.4 eV) and high crystal distortion of BiO_8 hybridization between the lone pair states of Bi-6s and the O-2p [54–56]. Various $BiVO_4$ synthesis methods have been reported in the literature, e.g. hydrothermal [57], sol-gel [58], co-precipitation [37, 59], sonochemical [60] etc., most of them use templates [61] or surfactants [62]. To avoid the latter, the researchers developed a green and sustainable synthesis without the assistance of any additives [63].

Herein, we synthesized monoclinic $BiVO_4$ by a simple precipitation process without using any organic solvents. The as-prepared powder was then heated at 400°C, 500°C, and 600°C, respectively. The obtained samples were characterized by X-ray powder diffraction (XRD), Raman spectroscopy, scanning electron microscopy (SEM), and UV-vis diffuse reflectance spectroscopy (DRS). Finally, the photodegradation activities were characterized by using the model organic pollutants of methylene blue (MB) and methyl orange (MO) under visible light illumination. The re-usability of the catalysts was determined in recycling tests, and the photocatalytic mechanism was unveiled by investigating the behavior of the photogenerated charge carriers.

Experimental

Materials

Bismuth nitrate pentahydrate ($Bi(NO_3)_3{\cdot}5H_2O$, 98%, Alfa Aesar), ammonium metavanadate (NH_4VO_3, 98%, ACROS Organics), nitric acid (HNO_3 65%, Merck), and sodium hydroxide (NaOH, 99%, Fisher Scientific) were used as received without any further purifications. All solutions were prepared by using de-ionized water as solvent.

Synthesis of $BiVO_4$

$BiVO_4$ was synthesized via a simple chemical precipitation method. First, solution A was obtained after the dissolution of Bi $(NO_3)_3{\cdot}5H_2O$ in diluted HNO_3 (2M), and then solution B of NH_4VO_3 dissolved in NaOH (2M) was added dropwise to the former under constant stirring (250 RPM). After 1 h stirring (250 RPM) the pH of the resulting yellow solution was adjusted to 5 by using NaOH (5M), and a yellow precipitate is formed under vigorous stirring (250 RPM) for 30 min. The final product was filtered and washed with the de-ionized water for several times, and dried at 80°C overnight [64]. The as-prepared $BiVO_4$ samples were prepared at 400°C, 500°C, and 600°C for 3 h under air [37].

Characterization of $BiVO_4$

X-ray diffraction (XRD) was used to identify the crystal structure of the samples by employing Cu Kα radiation (λ = 1.5406 Å) in a Rigaku Miniflex II powder diffractometer at a scan speed of 4° min^{-1} in the angular range from 2θ = 10° to 60°. The crystalline structure determination was done by Rietveld refinement using the FullProf Suite software package. Raman spectra were recorded using 532 nm laser excitation at 0.25 mW power in a SENTERRA II Raman spectrometer. The morphology of the $BiVO_4$ powders was characterized by scanning electron microscopy (SEM, Thermo-Fisher Scientific Apreo C) with an accelerating voltage of 10 kV. UV-vis measurements were carried out with a miniature fiber optic-based spectrometer (high resolution HR4000 USB spectrometer HR4000CGUV–vis-NIR, Ocean Optics) in the wavelength region of 200–800 nm using a DH-2000-BAL (Ocean Optics) Deuterium Tungsten Halogen light source [65].

Photocatalytic degradation experiments

The photocatalytic activity of $BiVO_4$ was examined by the removal of 5 ppm methylene blue (MB) and 5 ppm methyl orange (MO) in aqueous solution of pH = 5.4 and 5.8, respectively. First, the catalysts were stirred in the dye solutions in dark to reach the adsorption-desorption equilibrium, then the dispersions were irradiated in the visible light range by a 300 W Xenon lamp. At specified time periods, aliquots of 3 ml were taken and centrifuged at 13400 rpm for UV-vis analysis in the 400–800 nm wavelength range using a Shimadzu UV 2600 spectrophotometer. Radical trapping tests were done by using ethylenediamine disodium tetra-acetate (EDTA), isopropanol (IPA), and L-ascorbic acid as scavengers for the active species h^+, $^{\bullet}OH$, and $O_2^{\bullet-}$, respectively.

Determination of the point of zero charge (pzc)

The pH_{pzc} of the $BiVO_4$ surface was determined via the method reported by Al-Harahsheh [66]. A sample mass of 50 mg was weighted into six beakers each containing 50 ml of 0.1 M potassium nitrate (KNO_3) solution. The zero-point charge measurements curve was obtained after setting the $pH_{initial}$ of the beakers to 2.1, 4.0, 6.5, 8.7, 10.1, and 12.5 by adding either 0.1 M NaOH or 0.1 M HNO_3 solution dropwise.

Photoelectrochemical measurements

Photoelectrochemical studies were conducted using an Origalys ElectroChem electrochemical workstation in a three-electrode system, where working electrodes (WE) were obtained by drop-casting the samples onto indium tin oxide (ITO)/glass substrates. In a typical experiment, 10 mg photocatalyst powder was dispersed into 2 ml of absolute ethanol by ultrasonication for 15 min. After dropping 100 μl of the suspension onto $1 \times 1\,cm^2$ ITO/glass, the electrode was dried at 100°C for 5 h. Measurements were carried out in a 0.1 M sodium sulfate (Na_2SO_4) aqueous solution, using Ag/AgCl and platinum foil as reference and counter electrode, respectively. Visible light irradiation was done by a 300 W Xe lamp equipped with a 420 nm cut-off filter (λ > 420 nm). Transient photocurrent curves were recorded at a bias of 0.4 V, while Mott-Schottky measurements were carried out at a frequency of 200 Hz.

Results and discussion

Structural analysis of $BiVO_4$

Figure 1 shows the powder X-ray diffractograms of the $BiVO_4$ materials obtained through co-precipitation, then treated at 400°C–600°C for 3 h. The diffraction profiles were first compared to the well referenced $BiVO_4$ in the ICSD database. All characteristic peaks at 2θ = 18.7, 28.9, 30.6, 34.5, and 46.7° were indexed with a single-phase monoclinic scheelite $BiVO_4$ structure (ICSD datasheet File Card N°96–901-3437). The sharp diffraction peaks in the XRD patterns indicate the formation of a well crystallized $BiVO_4$. The average D crystallite size was calculated by the Scherrer formula:

$$D = \frac{k\lambda}{\beta\cos(\Theta)} \quad (1)$$

Where k is the Scherrer-constant set to k = 0.9, λ is the wavelength of the X-ray radiation (0.15406 nm), β refers to the full width at half maximum (FWHM) of each peak in radian determined through Gaussian peak fitting, and θ is the Bragg position.

The crystallite size was found to be 20, 24, and 30 nm for samples prepared at temperatures 400, 500, and 600°C, respectively, showing only a small variation with calcination temperature. This latter influences the crystal growth by welding primary particles together resulting in the formation of bigger particles.

It is known that crystallite size has a significant effect on the photocatalytic performance of $BiVO_4$ through surface area and the corresponding availability of active sites, the electron-hole recombination, and charge carrier behavior. The results indicate that crystallinity and the crystal size of $BiVO_4$ increased with heat treatment temperature from 400°C to 500°C and 600°C, which is in accordance with growth theory, i.e. high temperature promotes the increase of grain size [67, 68]. As a consequence, small particles at low temperatures exhibited large specific surface area, which, in turn, provides higher active site density [69]. Furthermore, small particle size implies shorter diffusion length, which is beneficial for charge carrier transport as photogenerated electrons and holes can reach the surface to take part in redox reactions (photocatalytic degradation) before recombination [70].

The formation of the monoclinic scheelite structure with the I2/b space group was confirmed in all samples by the Rietveld refinement of the XRD patterns (Table 1). The observed and the calculated XRD patterns of $BiVO_4$ heated at 400°C, 500°C, and 600°C, along with the corresponding difference curves, are shown in Supplementary Fig. S2a–c. The figures of merit characterizing the quality of the structural refinement are listed in Supplementary Table S1, and the refined atomic positions are shown in Supplementary Table S2.

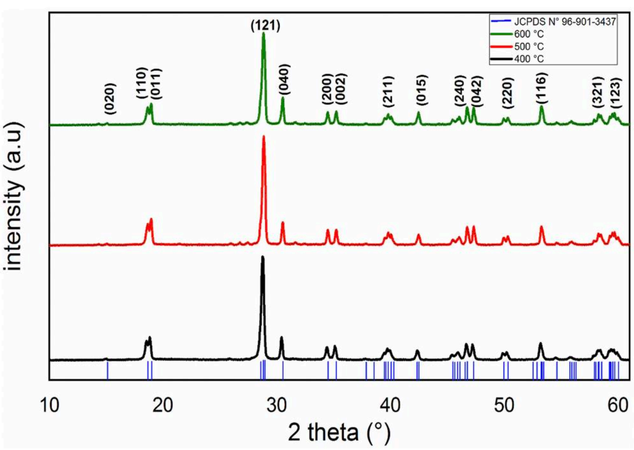

Figure 1. XRD pattern of BiVO4 samples prepared at 400, 500, and 600°C.

Table 1. Crystal structure data of $BiVO_4$ obtained at 400, 500, and 600°C.

Sample	400°C	500°C	600°C
Crystal system		Monoclinic	
Space group		I112/b	
Lattice parameters (Å)	a = 5.1866 (3) b = 5.0879 (4) c = 11.6873 (3)	a = 5.1912 (3) b = 5.0881 (4) c = 11.692 (3)	a = 5.1908 (6) b = 5.0868 (5) c = 11.691 (2)
γ (°)	90.3865 (4)	90.369 (3)	90.377 (5)
Volume ($Å^3$)	308.41	308.53	308.72

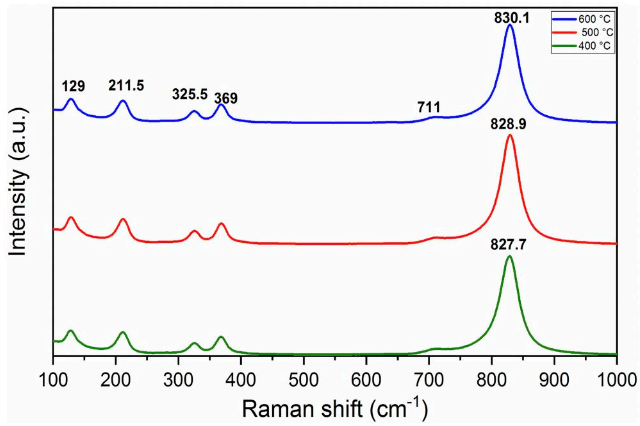

Figure 2. Raman spectra of BiVO4 prepared at 400, 500, and 600°C.

Vibrational analysis of $BiVO_4$

Figure 2 shows the Raman spectra of the samples prepared at 400°C, 500°C, and 600°C. The Raman shift at around 211.5, 325.5, 369, 711, and 830.1 cm^{-1} correspond to the monoclinic $BiVO_4$ according to the literature [71, 72]. The most intense bands centered at 827.7, 828.9, and 830.1 cm^{-1} referred to the symmetrical stretching mode of the V–O vibrations, while its anti-symmetric counterpart is located at 711 cm^{-1}. The bands at 369 and 325.5 cm^{-1} are the symmetric and asymmetric deformation modes of the VO_4^{3-} tetrahedron. Besides, the bands located at 211.5 and 129 cm^{-1} are the external modes in $BiVO_4$ involving rotation and translation. Therefore, results from Raman spectroscopy agree well with those from the previous XRD analysis [73, 74]. These findings are summarized in Table 2, where we can observe a red shift in the Raman bands positions with increasing calcination temperature. This behavior is due to the thermal expansion, bond population, less agitation of particles [75, 76].

Morphological analysis of $BiVO_4$

SEM images of $BiVO_4$ synthesized via the co-precipitation process after heat treatment at 400–600°C for 3 h were shown in Fig. 3. The sample obtained at 400°C consists of uniform spherically shaped particles (Fig. 3a), whereas agglomerated smaller particles are seen in the 500°C sample by assembling pseudospherical grains with distinct edges and facets (Fig. 3b and d). The 600°C heat treatment gave rise to more massive and dense assemblies in Fig. 3c. Thus, increasing calcination temperature in $BiVO_4$ led to an increase in particle size along with increasing

Table 2. Band identification in the Raman spectra of $BiVO_4$ heated at 400, 500, and 600°C.

Calcination temperature (°C)	Raman stretching frequency (cm^{-1})	Vibrational modes assignment	Refs
400 500 600	827.7 828.9 830.1	υ^s(V–O) Symmetric stretching V–O	
400	711	υ_{as}(V–O) Antisymmetric stretching V–O	[76–78]
500	369	$\delta_s(VO_4^{3-})$ Symmetric deformation V–O in VO_4^{3-}	
600	325.5	$\delta_{as}(VO_4^{3-})$ Antisymmetric deformation V–O in VO_4^{3-}	
	211.5 129	External modes (Rotation/Translation)	[101]

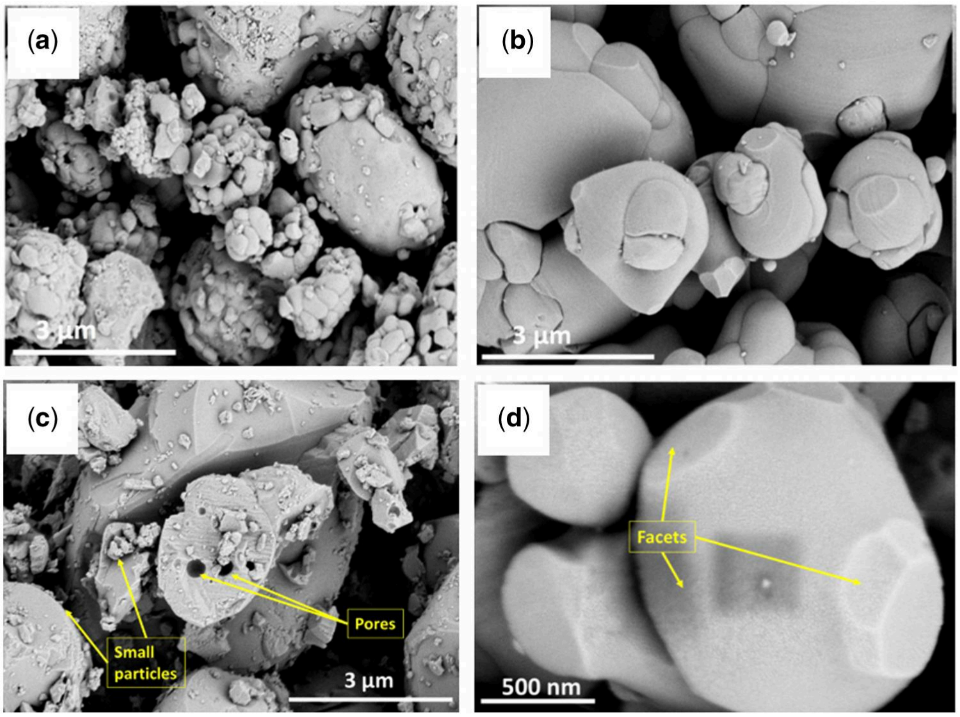

Figure 3. SEM micrographs of the BiVO4 obtained after calcination at (a) 400, (b) 500, and (c) 600°C. The 500°C sample at higher magnification where edges and facets are recognizable (d).

degree of particle agglomeration. Moreover, pores are also observed in each sample, at lower temperatures, probably microporosity due to surfaces defects and grain boundaries, followed by the formation of macroporosity by coalescence at 600°C.

UV-visible optical absorption of $BiVO_4$

Diffuse reflectance UV-vis spectroscopy (DRS) was utilized at room temperature to determine the optical properties of the $BiVO_4$ powders, and the optical spectra for $BiVO_4$ prepared at 400°C, 500°C, and 600°C are presented in Fig. 4a. The absorption onset wavelength of 480 nm corresponds to a band gap of 2.58 eV, which makes these catalysts suitable for visible light range application.

For a more precise band gap determination, the spectra were converted to the pseudo absorption function F(R) via the Kubelka–Munk relation (R) $= (1-R)^2/2R$, where R is the absolute reflectance. The Tauc plots, i.e. $(F(R)\ h\upsilon)^{1/n}$ versus the photon energy $h\upsilon$, were plotted (Fig. 4b), and band gaps E_g were calculated from the equation $(F(R)\ h\upsilon)^{1/n} = A\ (h\upsilon - Eg)$, where A is the proportionality constant, and n = ½ or 2 is a coefficient for direct and indirect band gap, respectively. Previous theoretical studies on the electronic structure of $BiVO_4$ found a direct band gap [77], i.e. the maximum of the valence band and the minimum of the conduction band are located at the same momentum. This allows the direct transition of excited electrons from the valence band to the conduction band as a result of photon absorption without any further assistance or change in the momentum [78–80]. In addition, band extrema are far from the center of the Brillouin zone, and the presence of Bi 6 s and O 2p causes an upward dispersion of the valence band at the zone boundary. Coupling V 3d, O 2p, and Bi 6p maintains a direct gap and lowers the conduction band minimum [81].

The band gap energies E_g were extracted from the linear fit of the Tauc plots of each sample [72], and Eg = 2.36, 2.38, and

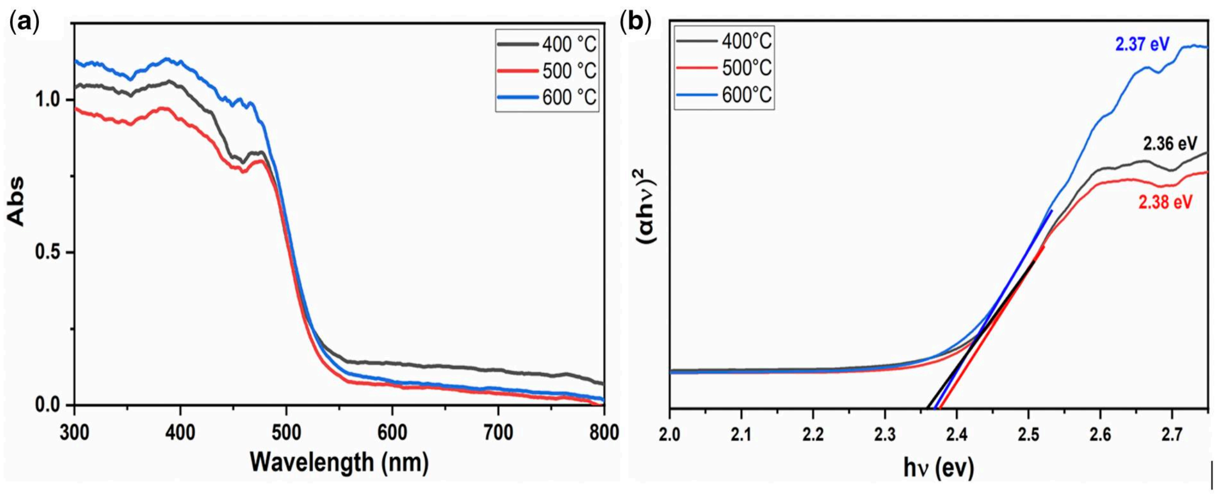

Figure 4. (a) UV-vis DRS spectra and (b) the corresponding Tauc plots of the BiVO4 samples obtained at 400, 500 and 600°C.

2.37 eV were obtained for the 400°C, 500°C, and 600°C samples, respectively. These results are in good agreement with previous literature results [37].

Optical absorption below 500 nm varies with calcination temperature. Absorbance of the sample treated at 400°C (black curve) is fairly high, reflecting strong light absorption in this region. Increasing the calcination temperature to 500°C (red curve), the absorbance drops, implying possible changes in the structure or morphology of the material, like reduction in defect density or change in grain size. Nevertheless, at 600°C (blue curve) the absorbance increases again and exceeds that of the 500°C sample. This is possibly due to enhanced crystallinity or particle aggregation that enhance the optical properties of the material.

Photocurrent analyses

The efficient charge carrier separation in the semiconductor is a prerequisite for a high photocatalytic performance, thus charge separation efficiency was investigated in transient photocurrent experiments (Fig. 5). The photocurrent response of $BiVO_4$ decreases with increasing calcination temperature, where the highest photocurrent density in $BiVO_4$ 400 implies a facilitated charge carrier separation. This decrease in photocurrent response with increase in calcination temperatures is a result of charge carrier recombination. Synthesis at high temperatures not only leads to increased crystallinity, but also to a reduction in the number of defects that serve as charge recombination centers [82]. Consequently, electron-hole recombination rates rise and reducing photocurrent intensity. Moreover, the well-preserved photocurrent density in the subsequent excitations indicates high photo-electrochemical stability. Calcination at 400°C resulted in the smallest crystallite size among the studied samples. This, on the one hand, increases the specific surface area, which provides more active site for pollutant adsorption, while on the other hand, give rise to a more pronounced crystal defect formation. The latter, in turn, deteriorates charge carrier mobility through unwanted photoinduced electron-hole recombination.

Photocatalytic activity of $BiVO_4$

The photocatalytic activity of $BiVO_4$ obtained at 400°C, 500°C, and 600°C was characterized by the decomposition of the model pollutants MB and MO dye molecules at room temperature under visible light illumination. The photocatalytic dye degradation

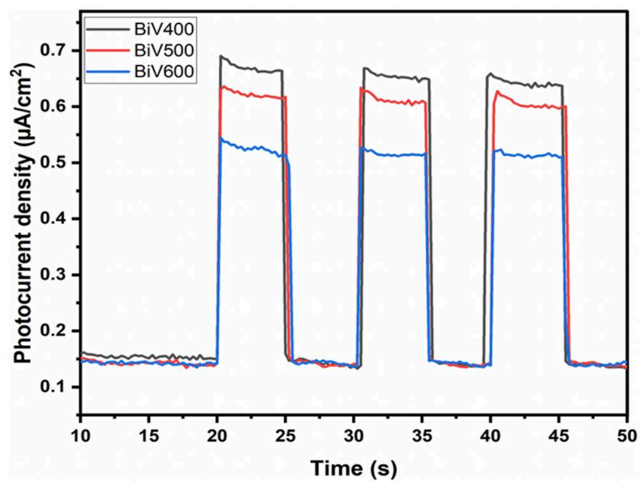

Figure 5. The transient photocurrent curves of BiVO4 prepared at 400, 500, and 600°C.

results are shown in Figs 6 and 7. In highly diluted solutions (ppm) the Beer-Lambert law applies, which means direct proportionality between the analyte concentration and the measured absorbance. The photocatalytic decomposition was followed by the change in the C_t/C_0 ratio with time, where C_t, C_0, and t are the dye concentration at the beginning of the experiment and at t reaction time (Figs 6b and 7b). Kinetic plots of the photodegradation reaction are constructed by plotting the negative logarithm of the former against time, and the dataset is fitted by a linear equation by using a pseudo-first-order model with the rate constant k [83]:

$$-\ln\frac{c_t}{c_0} = kt \quad (2)$$

Photocatalytic degradation of MB dye

Figure 6a shows the decreasing intensity of the absorption peak of MB at around 664 nm with increasing irradiation time in the presence of $BiVO_4$ (400°C). In the absence of irradiation, only 9% of the initial MB was decomposed after 1 h, which implies that dye removal is mainly the result of photocatalytic degradation rather than adsorption. Kinetic plots of the photodegradation

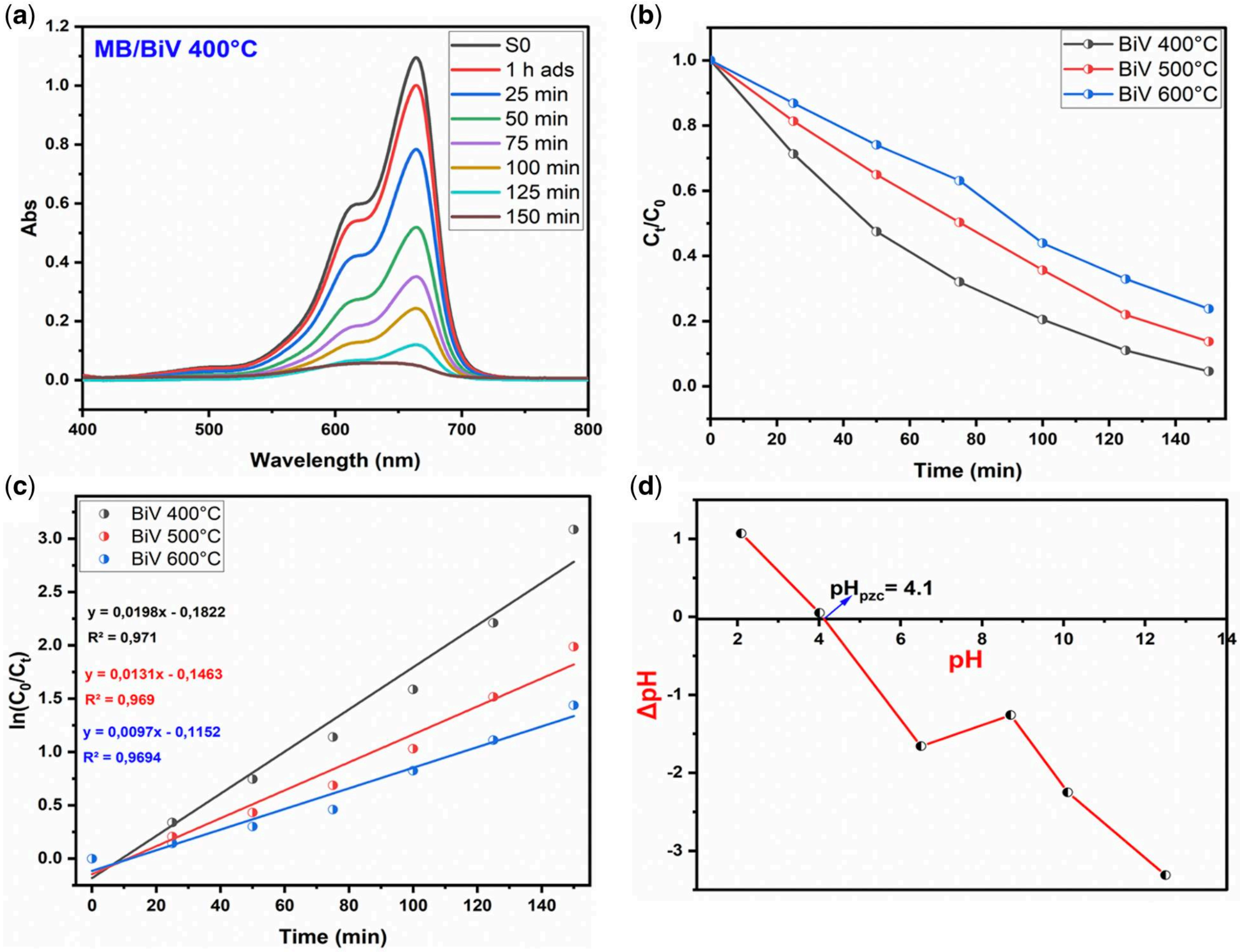

Figure 6. (a) UV-vis absorption spectra of MB during photocatalytic degradation on BiVO4 heated at 400°C, (b) variation of the Ct/C0 MB ratio over 150 min visible light irradiation, (c) the pseudo-first-order photodecomposition kinetics, and (d) Zero-point charge measurement for BiV400°C.

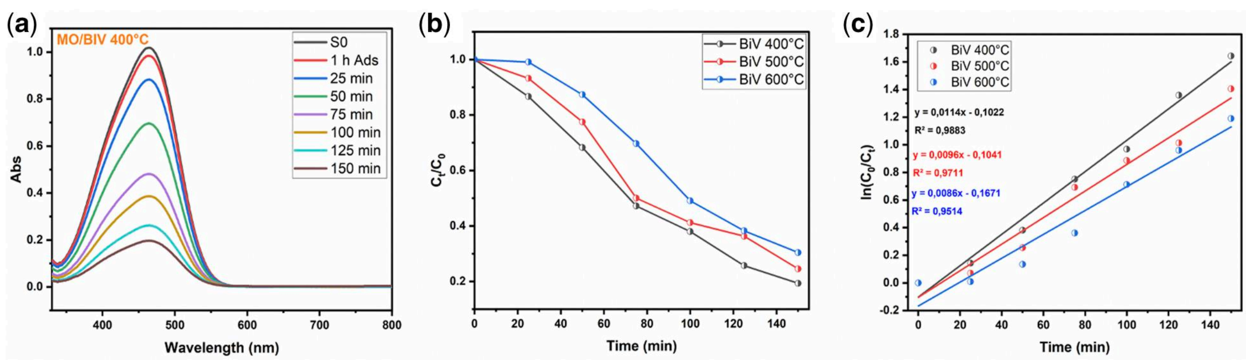

Figure 7. (a) UV-vis absorption spectra of MO during photocatalytic degradation on BiVO4 heated at 400°C, (b) variation of the Ct/C0 MO ratio over 150 min visible light irradiation on the BiVO4 catalysts prepared at 400, 500, and 600°C, (c) alongside with the pseudo-first-order photodecomposition kinetics.

reaction are depicted in Fig. 6b and c, where degradation kinetics was described by equation (2). $BiVO_4$ treated at 400°C shows the highest photocatalytic performance of 95% MB removal in 150 min, compared to those of $BiVO_4$ heated at 500°C (86%), and 600°C (76%). Pseudo-first order kinetic rate constants of $k = 0.0198$, 0.0131, and 0.0097 min^{-1} for $BiVO_4$ 400°C, 500°C, and 600°C are found, respectively (Fig. 6c). The poor photocatalytic performance of the samples heated at higher temperatures corroborates with the transient photocurrent results above, indicating rapid recombination of the photo induced charge carriers (Fig. 5). The catalytic activity of $BiVO_4$ 400°C is supported by its optical characteristics, particularly its narrow band gap along with higher visible light absorption and the small particle size with higher accessible surface area [5, 37, 84, 85]. Furthermore, it also depends on the point of zero charge (pH_{pzc}) of the catalyst, (Fig. 6d) influenced by the electrical charge and the state of the surface [86]. Results show, that $BiVO_4$ surfaces are negatively charged during the photocatalytic test reaction, as the pH of the dye solution (pH = 5.1) is higher than that of the pHpzc = 4.1. The electrostatic attraction between the negative charged catalyst surface and the positively charged cationic dye MB enhances dye adsorption, and consequently, improves photocatalytic activity.

The high degradation efficiency observed for $BiVO_4$ sample prepared at 400°C can be attributed to the combination of structural and morphological factors derived from crystallite size data and SEM analysis. Firstly, smaller crystallite size of 20 nm compared to that of 24 nm for BiV 500 and 30 nm for BiV 600, BiV 400 benefits from a larger specific surface area [87, 88]. This increases the number of active sites available for degradation reactions, enabling more effective interaction between the material and the molecules to be degraded [89, 90]. In addition, SEM analysis reveals that the particles at 400°C have a uniform, spherical morphology, which promotes homogeneous light scattering and better photon absorption. Moreover, band gap energy for BiV 400 is slightly lower than that for BiV 500 and BiV 600. Narrower band gap allows the material to absorb a wider range of wavelengths in the visible region, increasing its efficiency in photocatalytic reactions. Regarding photoelectrochemical performance, the photocurrent results show that BiV 400 exhibits the highest photocurrent density (Fig. 5), indicating high efficiency in separating photogenerated charges. In summary, the good performance of BiV 400 in terms of degradation is due to its small crystallite size, uniform morphology, and the corresponding high photocurrent. These factors enable stronger interaction with light and target molecules, in contrast to samples calcined at 500°C and 600°C.

Photocatalytic degradation of organic MO dye

Figure 7a shows the time dependent UV-vis absorption spectrum of MO with intensity maximum at 465 nm upon visible light irradiation using the $BiVO_4$ 400°C catalyst. The MO loss due adsorption was found to be only 4% in the dark after 1 h, which verifies that MO removal also takes places due photocatalytic degradation just like in the case of MB in 3.5.1. The corresponding kinetic curves are plotted in Fig. 7b and in their linearized form in Fig. 7c.

The photodegradation efficiency of 80% on $BiVO_4$ obtained at 400°C was the highest compared to those if 500°C (75%) and 600°C (69%) samples after 150 min visible light exposure. The kinetic constants were extracted from Fig. 7c using the pseudo-first order model of equation (2), and the corresponding k values were 0.0114, 0.0096, and 0.0086 min^{-1} for the $BiVO_4$ samples treated at 400, 500, and 600°C, respectively. Since the point of zero charge of $BiVO_4$ is pHpzc = 4.1 (Fig. 6d), the surface of the samples in the MO degradation measurements (pH = 3.1) is positively charged. The electrostatic attraction between the positively charged catalyst and the negative charge of the anionic dye, in turn, further promotes MO photo degradation.

The differences in the photocatalytic performance degrading MB and MO can be explained by their chemical properties and interactions with the photocatalyst. The different rates of photocatalytic decomposition of MB and MO may be attributable to the different electric charge of the dyes and the photocatalyst, along with the different molecular size of the dyes [91, 92]. The pH of the medium plays a crucial role in modulating the surface charge of the photocatalyst, thereby influencing its interaction with pollutants. The surface charge is mainly determined by the photocatalyst's point of zero charge (PZC). These variations in charge directly affect electrostatic interactions with contaminants. Therefore, pH optimization is essential to maximize the favorable interactions between the photocatalyst surface and the target pollutant, and thus to improve the overall performance of the photocatalytic process. On the other hand, the smaller molecular size of MB also promoted its faster and more complete photocatalytic decomposition. Moreover, –C=S– and –C=N– in the molecular structure of MB dissociate easily upon interacting with active species due to their low bond energy [91, 92], while photocatalytic decomposition of MO was hampered by the high dissociation energy of the –N=N– bonds in the MO structure [91, 92].

Trapping test and recyclability

Trapping tests were conducted for the determination of the major oxidizing species responsible for dye degradation. Ethylenediaminetetraacetic acid (EDTA), L-ascorbic acid (L-asc) and isopropanol alcohol (IPA) were selected as specific radical trap moieties for identifying any short-lived species potentially involved in MB and MO decomposition, i.e. h^+, $O_2^{\bullet-}$, and $^{\bullet}OH$. Figure 8a depicts the impacts of trapping agents on the photodegradation efficiency of MB and MO on the $BiVO_4$ 400°C catalyst. In the absence of trapping agents, the photocatalytic

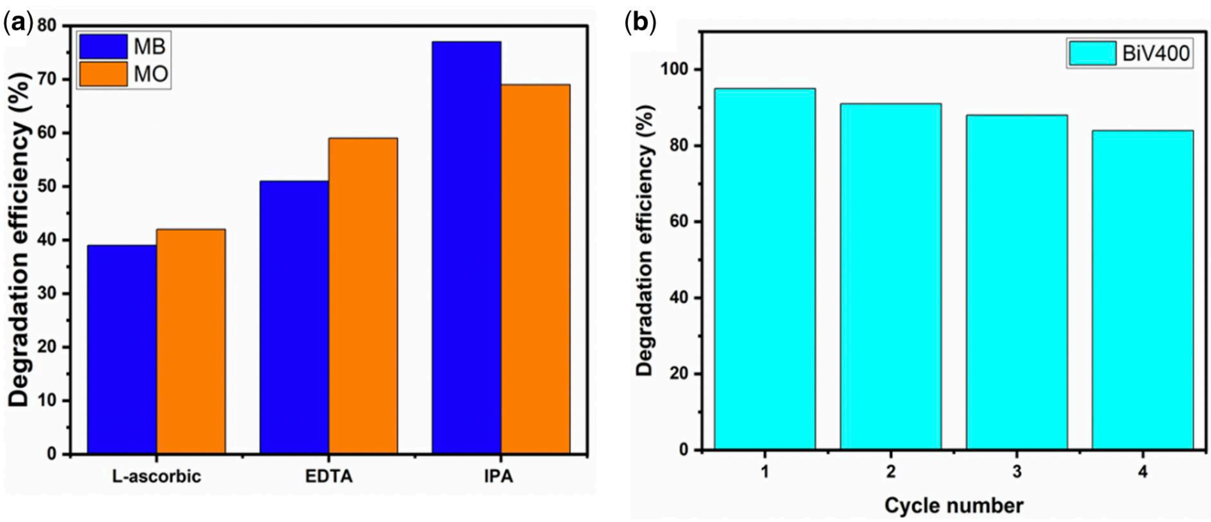

Figure 8. (a) Photocatalytic decomposition efficiency of MB and MO on BiVO4 400°C in the presence of trapping agents, and (b) photocatalyst recycling in four successive tests.

decomposition rates were 95% for MB and 80% for MO (**Figs 6 and 7**). Upon addition of L-ascorbic acid, EDTA, and IPA, the activities dropped to 39%, 51%, and 77% for MB and 42%, 59%, and 69% for MO, respectively. This indicates that holes h^+ and superoxide $O_2^{\bullet -}$ appear to be the major species in the photocatalytic decomposition of MB and MO, whereas hydroxyl radicals $^{\bullet}OH$ have a secondary role in the photocatalytic decomposition. The stability of the $BiVO_4$ 400°C sample was assessed by reusing the catalyst at the end of every photocatalytic reaction. The collected photocatalyst has been washed and then dried for subsequent reuse. The results in Fig. 8b show only a minor drop in the decomposition efficiency after 4 successive tests.

Proposed mechanism

The band gap of $BiVO_4$ 400°C, i.e. the energy difference of the band edges of the conduction (CB) and valence bands (VB), was determined from its optical properties in Fig. 4, whereas the band edge of the CB (the so-called flat-band potential) can be independently calculated from electrochemical measurements using the Mott-Schottky equation:

$$C^{-2} = \frac{2}{N_D e \varepsilon \varepsilon_0}\left(V - V_{fb} - \frac{kT}{e}\right) \tag{3}$$

where C is the interfacial capacitance, N_D is the carrier density, e is the electronic charge, ε and ε_0 is the dielectric constant of the semiconductor and the free space, V and V_{fb} is the applied and the flat band potential, k is the Boltzmann constant, and T is the absolute temperature.

Plotting C^{-2} against the applied potential, a linear trend is seen in a limited potential region in Fig. 9a. A positive slope of the latter indicates that the fabricated $BiVO_4$ 400°C is a n-type semiconductor, while fitting Equation (3) to these data provides its flat band potential (V_{fb}) from the x-intercept. The resulted V_{fb} = −0.61 V (versus. Ag/AgCl) can then be translated onto the normal hydrogen electrode scale (NHE) by $E_{Ag/AgCl=ENHE}$ - 0.197 [93, 94], however, it is known from the literature that conduction band potentials are more negative by 0.2 V than the measured V_{fb} flat band potential in n-type semiconductors [95–97]. Thus, the valence and conduction band edge positions in $BiVO_4$ 400 was calculated by the following equations:

$$E_{CB} = V_{fb} - 0.2 \tag{4}$$

$$E_g = E_{VB} - E_{CB} \tag{5}$$

From Equation (4) the E_{CB} value of – 0.81 V (versus. Ag/AgCl) is given, which equals to – 0.613 V (versus. NHE). The corresponding EVB = 1.74 (V versus. NHE) is derived from Equation (5) by adding E_{CB} and E_g, while the active species of the $BiVO_4$ 400°C photocatalyst are characterized by the potentials of the $E(H_2O/^{\bullet}OH)$ = (1.99 (V versus. NHE) and the $E(O_2/O_2^{\bullet -}) = -0.33$ (V versus. NHE) redox couples [98]. As can be seen in Fig. 9b, the CB edge potential is more negative compared to that of $O_2/O_2^{\bullet -}$, which in turn implies that the $BiVO_4$ 400°C catalyst is able to produce $O_2^{\bullet -}$. On the other hand, the VB edge potential is more negative than that of $H_2O/^{\bullet}OH$ making it difficult to generate $^{\bullet}OH$ radicals. As a consequence, $^{\bullet}OH$ radicals play a minor function in the degradation process [99–101]. This aligns well with the active moieties trapping results in Fig. 8, which showed that superoxide radicals are the major species responsible for degradation. The photocatalytic performance of various $BiVO_4$-based systems were collected from the literature, and their performance metrics are presented in Table 3 along with the experimental parameters of the tested model contaminants and the irradiation sources. The material developed in this study shows a high photocatalytic performance compared to the other reported $BiVO_4$-based photocatalysts.

Conclusions

$BiVO_4$ has been successfully prepared by a facile precipitation method without using any organic additives. The as-prepared materials were subjected to a subsequent calcination at 400, 500, and 600°C. It was found that the heat treatment had a significant impact on the structural, morphological, optical, and photocatalytic properties of the resulting $BiVO_4$. All synthesized samples possessed a single phase monoclinic scheelite structure with a uniform spherical particle morphology, where increasing calcination temperature resulted in an increase in the crystallite size. The bandgap of the semiconductor catalysts was determined by optical spectroscopy (Eg = 2.36 eV), which shows considerably visible light absorption and makes the catalyst suitable for sunlight activation. The $BiVO_4$ prepared at 400°C showed the highest photocatalytic activity among the studied materials, decomposing 95% and 80% of the initial methylene blue and methyl orange after 150 minutes of visible light illumination, respectively.

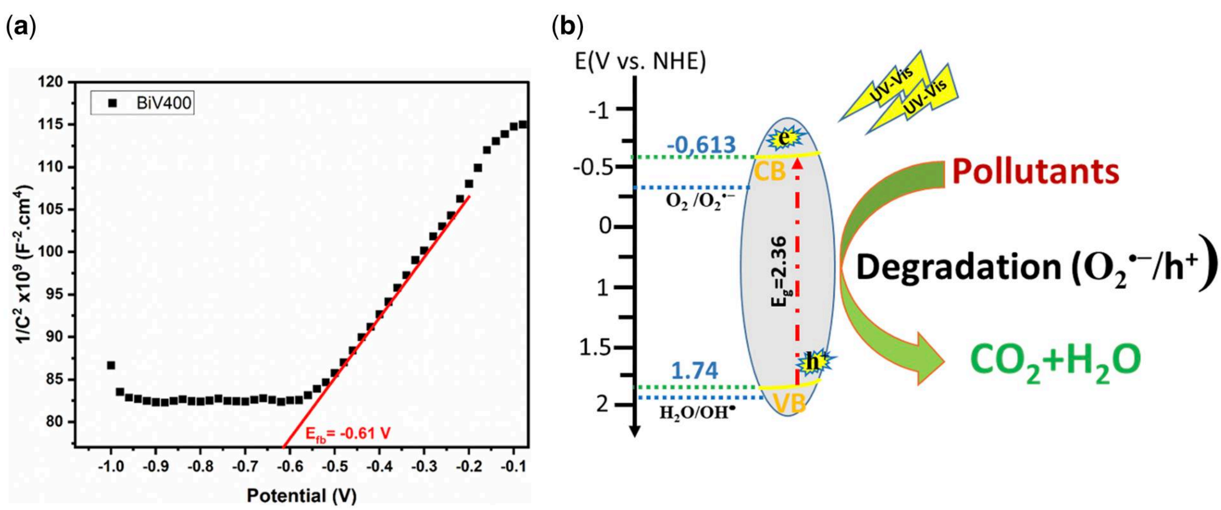

Figure 9. (a) Mott-Schottky graph of the BiVO4 400 photocatalyst, and (b) the scheme of the proposed degradation mechanism.

Table 3. A comparative analysis of the photocatalytic efficacy of the $BiVO_4$ photocatalyst with other reported photocatalysts.

Photocatalyst	Pollutant	Synthesis method	Concentration (mg/L)	Light sources (W)	Efficiency	Ref
1 wt% Pd/$BiVO_4$	MO	Impregnation	10	Lamp (12 W)	100% 15 h	[102]
$BiVO_4$-1	MO	hydrothermal	10	Xe lamp (300 W)	44% 4 h	[103]
$BiVO_4$-2					60% 4 h	
$BiVO_4$-3					68% 4 h	
$BiVO_4$-4					87% 4 h	
0.04 mol% B/$BiVO_4$	MO	Sol gel	10	Halogen lamp (250 W)	98% 50 min	[104]
6.5 wt% Ag/$BiVO_4$	MB	Hydrothermal	5	Xe lamp (350 W)	98% 6 h	[105]
$BiVO_4$ + Peroxymonosulfate (PMS) + Visible	MB	Hydrothermal	5	LED light	99% 90 min	[106]
0 wt%-$BiVO_4$–paint					27% 240 min	[107]
20 wt%-$BiVO_4$–paint	MB	Coating	5	2 Havells bulbs (15 w)	67% 240 min	
40wt%-$BiVO_4$–paint					72% 240 min	
$BiVO_4$ 400°C	MB	Co-precipitation	5	Philips lamps (300 W)	95% 150 min	This study
	MO				80% 150 min	

Moreover, the same sample provided the highest photocurrent density implying an effective charge carrier separation. Finally, the trapping experiment indicated that the primary reactive species utilized in the photocatalytic degradation of MB and MO are holes (h^+) and superoxide ($O_2^{\bullet-}$), which corroborated well with the band structure determination. In conclusion, $BiVO_4$ is a promising visible-light semiconductor photocatalyst for various applications, such as hydrogen production, degradation of organic pollutants in water and volatile organic compounds (VOCs). However, several challenges still need to be resolved, like fast charge carrier recombination, low electric conductivity, and the cost-effective synthesis. To that end, several strategies (controlling the kinetics and morphology, surface modification and doping, fabricating heterostructures and depositing co-catalysts) were employed to enhance the photocatalytic performance.

Authors declare no conflict of interest.

Acknowledgements

Safia Lotfi thanks the support of CNRST (Centre National pour la Recherche Scientifique et Technique) in the Excellence Research Scholarships Program. The authors are thankful to the faculty of Science, Mohammed V University in Rabat, Morocco. Prof.s. Ait Ahsaine and Madjid thank the IM2NP for the characterization of the prepared materials.

Author contributions

Safia Lotfi (Conceptualization [equal], Data curation [equal], Formal analysis [equal], Investigation [equal], Methodology [equal], Software [equal], Visualization [equal], Writing—original draft [equal], Writing—review & editing [equal]), Mohamed El Ouardi (Data curation [equal], Formal analysis [equal], Investigation [equal], Software [equal], Validation [equal], Visualization [equal], Writing—original draft [equal], Writing—review & editing [equal]), Madjid Arab (Data curation [equal], Formal analysis [equal], Validation [equal], Writing—original draft [equal], Writing—review & editing [equal]), Abderrazzak Assani (Conceptualization [equal], Formal analysis [equal], Investigation [equal], Methodology [equal], Project administration [equal], Supervision [equal], Validation [equal], Writing—original draft [equal], Writing—review & editing [equal]), Amal BaQais (Data curation [equal], Formal analysis [equal], Investigation [equal], Writing—original draft [equal], Writing—review & editing [equal]), Henrik Haspel (Funding acquisition [equal], Methodology [equal], Validation [equal], Writing—original draft [equal], Writing—review & editing [equal]), Zoltán Kónya (Funding acquisition [equal], Project administration [equal], Supervision [equal], Writing—review & editing [equal]), and Hassan Ait Ahsaine (Conceptualization [equal], Formal analysis [equal], Investigation [equal], Methodology [equal], Project administration [equal], Supervision [equal], Validation [equal], Writing—original draft [equal], Writing—review & editing [equal])

Supplementary data

Supplementary data is available at *OXFMAT Journal* online.

Conflict of interest: None declared.

Funding

H.H. thanks the financial support of the János Bolyai Research Grant of the Hungarian Academy of Sciences (BO/682/22). Z.K. is grateful for the K 21 138714 and SNN_135918 projects of the National Research, Development and Innovation Fund. TKP2021-NVA-19 under the TKP2021-NVA funding scheme of the Ministry for Innovation and Technology are acknowledged. Project no. RRF-2.3.1–21-2022-00009 (National Laboratory for Renewable Energy) was undertaken with the support provided by the Recovery and Resilience Facility of the European Union within the framework of Programme Széchenyi Plan Plus. The project received funding from the HUN-REN Hungarian Research Network. Dr BaQais thanks Princess Nourah bint Abdulrahman University Researchers Supporting Project number (PNURSP2025R230), Princess Nourah bint Abdulrahman University, Riyadh, Saudi Arabia.

Data availability

The data underlying this article will be shared on reasonable request to the corresponding author.

References

1. Duy Nguyen T, Cao VD, Huu Nguyen V *et al.* Synthesized $BiVO_4$ was by the co-precipitation method for Rhodamine B degradation under visible light. *IOP Conf Ser: Mater Sci Eng* 2019;**542**: 012058. https://doi.org/10.1088/1757-899X/542/1/012058
2. Trinh DTT, Khanitchaidecha W, Channei D, Nakaruk A. Synthesis, characterization and environmental applications of bismuth vanadate. *Res Chem Intermed* 2019;**45**:5217–59. https://doi.org/10.1007/s11164-019-03912-2
3. Samsudin MFR, Sufian S, Hameed BH. Epigrammatic progress and perspective on the photocatalytic properties of $BiVO_4$-based photocatalyst in photocatalytic water treatment technology: A review. *J Mol Liq* 2018;**268**:438–59. https://doi.org/10.1016/j.molliq.2018.07.051
4. Qamar MA, Shahid S, Javed M *et al.* Accelerated decoloration of organic dyes from wastewater using ternary metal/g-C3N4/ZnO nanocomposites: an investigation of impact of g-C3N4 concentration and Ni and Mn doping. *Catalysts* 2022;**12**: 1388. https://doi.org/10.3390/catal12111388
5. Lotfi S, Ouardi ME, Ahsaine HA, Assani A. Recent progress on the synthesis, morphology and photocatalytic dye degradation of BiVO 4 photocatalysts: a review. *Catal Rev* 2024;**66**: 214–58. https://doi.org/10.1080/01614940.2022.2057044
6. El Allaoui B, Chakhtouna H, Zari N *et al.* Superhydrophobic alkylsilane functionalized cellulose beads for efficient oil/water separation. *J Water Process Eng* 2023;**54**:104015. https://doi.org/10.1016/j.jwpe.2023.104015
7. Farsad S, Amjlef A, Chaoui A *et al.* Harnessing a carbon-based material from food waste digestate for dye adsorption: the role of hydrogel beads in enhancing the material stability and regenerative capacity. *Mater Adv* 2023;**4**:6599–611. https://doi.org/10.1039/D3MA00505D
8. Channab B-E, El Ouardi M, Marrane SE *et al.* Alginate@ZnCO2O4 for efficient peroxymonosulfate activation towards effective rhodamine B degradation: optimization using response surface methodology. *RSC Adv* 2023;**13**: 20150–63. https://doi.org/10.1039/D3RA02865H
9. Lin L, Yang H, Xu X. Effects of water pollution on human health and disease heterogeneity: a review. *Front Environ Sci* 2022;**10**:880246. https://doi.org/10.3389/fenvs.2022.880246
10. El Idrissi A, El Gharrak A, Achagri G *et al.* Synthesis of urea-containing sodium alginate-g-poly(acrylic acid-co-acrylamide) superabsorbent-fertilizer hydrogel reinforced with carboxylated cellulose nanocrystals for efficient water and nitrogen utilization. *J Environ Chem Eng* 2022;**10**:108282. https://doi.org/10.1016/j.jece.2022.108282
11. Achagri G, Idrissi AE, Majdoub M *et al.* Octadecylamine-functionalized cellulose nanocrystals as durable superhydrophobic surface modifier for polyester coating: towards oil/water separation. *Results in Surfaces and Interfaces* 2022;**8**:100061. https://doi.org/10.1016/j.rsurfi.2022.100061
12. Precious Sibiya N, Rathilal S, Kweinor Tetteh E. Coagulation treatment of wastewater: kinetics and natural coagulant evaluation. *Molecules* 2021;**26**:698. https://doi.org/10.3390/molecules26030698
13. Zhang X-H. The study on flocculation treating wastewater from domestic animals and poultry breeding. *IERI Procedia* 2014;**9**:2–7. https://doi.org/10.1016/j.ieri.2014.09.032
14. Huang X, Guida S, Jefferson B, Soares A. Economic evaluation of ion-exchange processes for nutrient removal and recovery from municipal wastewater. *NPJ Clean Water* 2020;**3**:7. https://doi.org/10.1038/s41545-020-0054-x
15. Wang LK, Vaccari DA, Li Y, Shammas NK (eds). Chemical precipitation. In: *Physicochemical Treatment Processes*, Handbook of Environmental Engineering. Totowa, NJ: Humana Press, Springer Nature, 2005, 141–97. https://doi.org/10.1385/1-59259-820-x : 141
16. Ospanov K, Kuldeyev E, Kenzhaliyev B, Korotunov A. Wastewater treatment methods and sewage treatment facilities in Almaty, Kazakhstan. *J Ecol Eng* 2022;**23**:240–51. https://doi.org/10.12911/22998993/143939
17. Mircea N (ed.). 11 Waste water disinfection. Waste water and sludge chlorination for various purposes. In: *Municipal Waste Water Treatment*, 1985, 438–56. https://doi.org/10.1016/S0167-5648(08)71093-1
18. Paździor K, Bilińska L, Ledakowicz S. A review of the existing and emerging technologies in the combination of AOPs and biological processes in industrial textile wastewater treatment. *Chem Eng J* 2019;**376**:120597. https://doi.org/10.1016/j.cej.2018.12.057
19. Chakravorty A, Roy S. A review of photocatalysis, basic principles, processes, and materials. *Sustain Chem Environ* 2024;**8**: 100155. https://doi.org/10.1016/j.scenv.2024.100155
20. Hoffmann MR, Martin ST, Choi W, Bahnemann DW. Environmental applications of semiconductor photocatalysis. *Chem Rev* 1995;**95**:69–96. https://doi.org/10.1021/cr00033a004
21. Zhao Z. Research progress of semiconductor photocatalysis applied to environmental governance. *IOP Conf Ser: Earth Environ Sci* 2021;**631**:012022. https://doi.org/10.1088/1755-1315/631/1/012022
22. Li W, Kong D, Yan T *et al.* Alkali-treatment synthesis of bismuth vanadium oxide photocatalysts with different morphologies. *J Solid State Chem* 2020;**286**:121296. https://doi.org/10.1016/j.jssc.2020.121296
23. Belver C, Bedia J. Structured semiconductors in photocatalysis. *Catalysts* 2023;**13**:1111. https://doi.org/10.3390/catal13071111
24. Zhang K, Deng J, Liu Y *et al.* Photocatalytic removal of organics over BiVO4-based photocatalysts. *Semicond Photocatal Mater Mech Appl* 2016;**21**:559–611. https://doi.org/10.5772/62745
25. Channab B-E, El Ouardi M, Ait Layachi O *et al.* Recent trends on MIL-Fe metal–organic frameworks: synthesis approaches, structural insights, and applications in organic pollutant adsorption and photocatalytic degradation. *Environ Sci: Nano* 2023;**10**:2957–88. https://doi.org/10.1039/D3EN00332A
26. Mohammadi H, Kazemi Z, Aghaee A *et al.* Unraveling the influence of TiO2 nanoparticles on growth, physiological and phytochemical characteristics of Mentha piperita L. in cadmium-contaminated soil. *Sci Rep* 2023;**13**:22280. https://doi.org/10.1038/s41598-023-49666-1
27. Stephen L. Titanium dioxide versatile solid crystalline: an overview. In: Dongre R, Peshwe DR (eds), *Assorted Dimensional*

Reconfigurable Materials. London UK: IntechOpen, 2020. https://doi.org/10.5772/intechopen.92056

28. Wu Q, Han R, Chen P *et al.* Novel synthesis and photocatalytic performance of BiVO4 with tunable morphologies and macroscopic structures. *Mater Sci Semicond Process* 2015;**38**:271–7. https://doi.org/10.1016/j.mssp.2015.04.040
29. Xie Z, Zhang Y, Liu X *et al.* Visible light photoelectrochemical properties of N-Doped TiO2 nanorod arrays from TiN. *J Nanomater* 2013;**2013**:1–8. https://doi.org/10.1155/2013/930950
30. Tan JZY, Maroto-Valer MM. A review of nanostructured non-titania photocatalysts and hole scavenging agents for CO2 photoreduction processes. *J Mater Chem A* 2019;**7**:9368–85. https://doi.org/10.1039/C8TA10410G
31. Shi W, Bao Yu CS. Research progress on the molecular structure of amorphous chalcogen elements. *Chem J Chinese Univ* 2024;**45**:20240054(14/14). https://doi.org/10.7503/cjcu20240054
32. Yao X, Zhang D, Liu Y *et al.* One stone, three birds: up-conversion, photothermal and p-n heterojunction to boost BiOBr: Yb3+,Er3+/Cu3Mo2O9 full spectrum photodegradation. *Front Chem Sci Eng* 2024;**18**:118. https://doi.org/10.1007/s11705-024-2469-2
33. Li Y, Zeng Z, Chen Y *et al.* $FeVO_4$ nanowires for efficient photocatalytic CO_2 reduction. *Catal Sci Technol* 2022;**12**:3289–94. https://doi.org/10.1039/D2CY00324D
34. Huang C, Chen L, Li H *et al.* Synthesis and application of Bi2WO6 for the photocatalytic degradation of two typical fluoroquinolones under visible light irradiation. *RSC Adv* 2019;**9**:27768–79. https://doi.org/10.1039/C9RA04445K
35. Yao B, Zheng G, Luan Y *et al.* Cost-effective Bi2WO6 for efficient degradation of rhodamine B and tetracycline. *J Mater Sci Mater Electron* 2023;**34**:246. https://doi.org/10.1007/s10854-022-09654-z
36. Zahid AH, Han Q. A review on the preparation, microstructure, and photocatalytic performance of Bi2O3 in polymorphs. *Nanoscale* 2021;**13**:17687–724. https://doi.org/10.1039/D1NR03187B
37. Ganeshbabu M, Kannan N, Venkatesh PS *et al.* Synthesis and characterization of BiVO4 nanoparticles for environmental applications. *RSC Adv* 2020;**10**:18315–22. https://doi.org/10.1039/D0RA01065K
38. Bhanderi D, Lakhani P, Modi CK. Graphitic carbon nitride (g-C3N4) as an emerging photocatalyst for sustainable environmental applications: a comprehensive review. *RSC Sustain* 2024;**2**:265–87. https://doi.org/10.1039/D3SU00382E
39. Sivakumar V, Suresh R, Giribabu K, Narayanan V. Solventless synthesis of m-LaVO4 photocatalyst for the degradation of methylene blue and textile effluent. *J Mater Sci: Mater Electron* 2017;**28**:4014–9. https://doi.org/10.1007/s10854-016-6014-z
40. Zonarsaghar A, Mousavi-Kamazani M, Zinatloo-Ajabshir S. Sonochemical synthesis of CeVO4 nanoparticles for electrochemical hydrogen storage. *Int J Hydrogen Energy* 2022;**47**:5403–17. https://doi.org/10.1016/j.ijhydene.2021.11.183
41. Albukhari SM. Silver vanadate-coupled yttrium orthovanadate nanocomposite: an improved photocatalyst for amended visible-light-driven hydrogen evolution. *Opt Mater (Amst)* 2023;**144**:114383. https://doi.org/10.1016/j.optmat.2023.114383
42. Saison T, Chemin N, Chanéac C *et al.* Bi_2O_3, $BiVO_4$, and Bi_2WO_6: impact of surface properties on photocatalytic activity under visible light. *J Phys Chem C* 2011;**115**:5657–66. https://doi.org/10.1021/jp109134z
43. Jiang S, Wang L, Hao W *et al.* Visible-light photocatalytic activity of S-doped α-Bi2O3. *J Phys Chem C* 2015;**119**:14094–101. https://doi.org/10.1021/jp5117036
44. Han A, Sun J, Chuah GK, Jaenicke S. Enhanced p-cresol photodegradation over BiOBr/Bi2O3 in the presence of rhodamine B. *RSC Adv* 2017;**7**:145–52. https://doi.org/10.1039/C6RA24852G
45. Utami BA, Sutanto H, Hidayanto E. Recent advances in doped Bi2O3 and its photocatalytic activity: a review. *Int J Res Rev* 2022;**9**:216–30. https://doi.org/10.52403/ijrr.20220128
46. Dou W, Hu X, Kong L, Peng X. Photo-induced dissolution of Bi2O3 during photocatalysis reactions: mechanisms and inhibition method. *J Hazard Mater* 2021;**412**:125267. https://doi.org/10.1016/j.jhazmat.2021.125267
47. Gao Y, Zhu S, Wang Z *et al.* Visible-driven photocatalytic activity and stability of Bi2O3 enhanced by CQDs. *J Mater Sci* 2024;**59**:19492–507. https://doi.org/10.1007/s10853-024-10327-x
48. Luévano-Hipólito E, Torres-Martínez LM, Cantú-Castro LVF. Self-cleaning coatings based on fly ash and bismuth-photocatalysts: Bi2O3, Bi2O2CO3, BiOI, BiVO4, BiPO4. *Constr Build Mater* 2019;**220**:206–13. https://doi.org/10.1016/j.conbuildmat.2019.06.030
49. Stefa S, Zografaki M, Dimitropoulos M *et al.* High surface area g-C3N4 nanosheets as superior solar-light photocatalyst for the degradation of parabens. *Appl Phys A* 2023;**129**:754. https://doi.org/10.1007/s00339-023-07032-y
50. Luo Y, Zhu Y, Han Y *et al.* g-C3N4-based photocatalysts for organic pollutant removal: a critical review. *Carbon Res* 2023;**2**:14. https://doi.org/10.1007/s44246-023-00045-5
51. Lv K, Wan D, Zheng D *et al.* Enhancement of visible light photocatalytic activity of BiVO4 by polypyrrole modification. *J Alloys Compd* 2021;**872**:159597. https://doi.org/10.1016/j.jallcom.2021.159597
52. Abdi FF, van de Krol R. Nature and light dependence of bulk recombination in Co-Pi-catalyzed BiVO4 photoanodes. *J Phys Chem C* 2012;**116**:9398–404. https://doi.org/10.1021/jp3007552
53. Monfort O, Plesch G. Bismuth vanadate-based semiconductor photocatalysts: a short critical review on the efficiency and the mechanism of photodegradation of organic pollutants. *Environ Sci Pollut Res Int* 2018;**25**:19362–79. https://doi.org/10.1007/s11356-018-2437-9
54. Le PH, Kien NT, Van CN. Recent advances in BiVO4- and Bi2Te3-based materials for high efficiency-energy applications. In: *Bismuth—Advanced Applications and Defects Characterization*., InTech, 2018. https://doi.org/10.5772/intechopen.75613
55. Wang Z, Xuan J, Liu B, He J. Photocatalytic degradation of C.I. reactive blue 19 by using novel nano BiVO 4 -coated cotton fabric. *J Ind Text* 2015;**44**:868–83. https://doi.org/10.1177/1528083713518088
56. Kudo A, Omori K, Kato H. A novel aqueous process for preparation of crystal form-controlled and highly crystalline BiVO4 powder from layered vanadates at room temperature and its photocatalytic and photophysical properties. *J Am Chem Soc* 1999;**121**:11459–67. https://doi.org/10.1021/ja992541y
57. Mansha MS, Iqbal T, Farooq M *et al.* Facile hydrothermal synthesis of BiVO4 nanomaterials for degradation of industrial waste. *Heliyon* 2023;**9**:e15978. https://doi.org/10.1016/j.heliyon.2023.e15978
58. Randive SG, Kore RM, Lokhande BJ. Sol-gel synthesis and supercapacitive characterization of bismuth vanadate. *J Nano- Electron Phys* 2020;**12**:02027-1–02027-4. https://doi.org/10.21272/jnep

59. Yu J, Zhang Y, Kudo A. Synthesis and photocatalytic performances of BiVO4 by ammonia co-precipitation process. *J Solid State Chem* 2009;**182**:223–8. https://doi.org/10.1016/j.jssc.2008.10.021
60. Kansaard T, Pecharapa W. Characterization of BiVO4 nanoparticles prepared by sonochemical process. *Ferroelectrics* 2019;**552**:140–7. https://doi.org/10.1080/00150193.2019.1653090
61. Jia Y, Yin G, Zhang C *et al.* Facile synthesis of BiVO4 nanorods by a template method. *Chem Lett* 2022;**51**:345–7. https://doi.org/10.1246/cl.210682
62. Montañés L, Mesa CA, Gutiérrez-Blanco A *et al.* Facile surfactant-assisted synthesis of BiVO4 nanoparticulate films for solar water splitting. *Catalysts* 2021;**11**:1244. https://doi.org/10.3390/catal11101244
63. Kamble GS, Ling Y-C. Solvothermal synthesis of facet-dependent BiVO4 photocatalyst with enhanced visible-light-driven photocatalytic degradation of organic pollutant: assessment of toxicity by zebrafish embryo. *Sci Rep* 2020;**10**:12993. https://doi.org/10.1038/s41598-020-69706-4
64. Liu X, Li JK. Effect of pH on the properties of BiVO4 by hydrothermal synthesis method. *SSP* 2018;**281**:813–8. https://doi.org/10.4028/www.scientific.net/SSP.281.813
65. Yunianto M, Qaulan Tsaqiila F, Anwar F, Endah Saraswati T. Detection of lard contents using fiber optic sensors. *J Phys: Conf Ser* 2021;**1825**:012077. https://doi.org/10.1088/1742-6596/1825/1/012077
66. Al-Harahsheh M, Shawabkeh R, Al-Harahsheh A *et al.* Surface modification and characterization of Jordanian kaolinite: application for lead removal from aqueous solutions. *Appl Surf Sci* 2009;**255**:8098–103. https://doi.org/10.1016/j.apsusc.2009.05.024
67. Abo El-Yazeed WS, El-Hakam SA, Salah AA, Ibrahim AA. Fabrication and characterization of reduced graphene-BiVO4 nanocomposites for enhancing visible light photocatalytic and antibacterial activity. *J Photochem Photobiol A Chem* 2021;**417**:113362. https://doi.org/10.1016/j.jphotochem.2021.113362
68. Saputera WH, Amri AF, Mukti RR *et al.* Photocatalytic degradation of palm oil mill effluent (POME) waste using BiVO4 based catalysts. *Molecules* 2021;**26**:6225. https://doi.org/10.3390/molecules26206225
69. Shi L, Zhuo S, Abulikemu M *et al.* Annealing temperature effects on photoelectrochemical performance of bismuth vanadate thin film photoelectrodes. *RSC Adv* 2018;**8**:29179–88. https://doi.org/10.1039/C8RA04887H
70. Zhang L, Dai Z, Zheng G *et al.* Superior visible light photocatalytic performance of reticular BiVO4 synthesized via a modified sol–gel method. *RSC Adv* 2018;**8**:10654–64. https://doi.org/10.1039/C8RA00554K
71. Ribeiro FWP, Gromboni MF, Marken F, Mascaro LH. Photoelectrocatalytic properties of BiVO4 prepared with different alcohol solvents. *Int J Hydrogen Energy* 2016;**41**:17380–9. https://doi.org/10.1016/j.ijhydene.2016.07.159
72. Merupo V-I, Velumani S, Ordon K *et al.* Structural and optical characterization of ball-milled copper-doped bismuth vanadium oxide (BiVO4). *CrystEngComm* 2015;**17**:3366–75. https://doi.org/10.1039/C5CE00173K
73. Thalluri SRM, Martinez-Suarez C, Virga A *et al.* Insights from crystal size and band gap on the catalytic activity of monoclinic $BiVO_4$. *IJCEA* 2013;305–9. https://doi.org/10.7763/IJCEA.2013.V4.315
74. Wang L, Liu J, Song W *et al.* Experimental and DFT insights of BiVO4 as an effective photocatalytic catalyst for N2O decomposition. *Chem Eng J* 2019;**366**:504–13. https://doi.org/10.1016/j.cej.2019.02.038
75. Xie S, Iglesia E, Bell AT. Effects of temperature on the Raman spectra and dispersed oxides. *J Phys Chem B* 2001;**105**:5144–52. https://doi.org/10.1021/jp004434s
76. Raravikar NR, Keblinski P, Rao AM *et al.* Temperature dependence of radial breathing mode Raman frequency of single-walled carbon nanotubes. *Phys Rev B* 2002;**66**:235424. https://doi.org/10.1103/PhysRevB.66.235424
77. Prakash J, Nechiyil D, Ali K *et al.* Band gap and defect engineering of bismuth vanadate using La, Ce, Zr dopants to obtain a photoelectrochemical system for ultra-sensitive detection of glucose in blood serum. *Dalton Trans* 2023;**52**:1989–2001. https://doi.org/10.1039/D2DT03304F
78. Kunzelmann VF, Jiang C-M, Ihrke I *et al.* Solution-based synthesis of wafer-scale epitaxial BiVO 4 thin films exhibiting high structural and optoelectronic quality. *J Mater Chem A Mater* 2022;**10**:12026–34. https://doi.org/10.1039/D1TA10732A
79. Makuła P, Pacia M, Macyk W. How to correctly determine the band gap energy of modified semiconductor photocatalysts based on UV–vis spectra. *J Phys Chem Lett* 2018;**9**:6814–7. https://doi.org/10.1021/acs.jpclett.8b02892
80. Sarker HP, Rao PM, Huda MN. Niobium doping in $BiVO_4$: interplay between effective mass, stability, and pressure. *ChemPhysChem* 2019;**20**:773–84. https://doi.org/10.1002/cphc.201800792
81. Gesesse GD, Gomis-Berenguer A, Barthe M-F, Ania CO. On the analysis of diffuse reflectance measurements to estimate the optical properties of amorphous porous carbons and semiconductor/carbon catalysts. *J Photochem Photobiol A Chem* 2020;**398**:112622. https://doi.org/10.1016/j.jphotochem.2020.112622
82. Maarisetty D, Baral SS. Defect engineering in photocatalysis: formation, chemistry, optoelectronics, and interface studies. *J Mater Chem A* 2020;**8**:18560–604. https://doi.org/10.1039/D0TA04297H
83. Zhang K, Liu Y, Deng J *et al.* Co–Pd/BiVO4: high-performance photocatalysts for the degradation of phenol under visible light irradiation. *Appl Catal B Environ* 2018;**224**:350–9. https://doi.org/10.1016/j.apcatb.2017.10.044
84. Kamble GS, Natarajan TS, Patil SS *et al.* BiVO4 as a sustainable and emerging photocatalyst: synthesis methodologies, engineering properties, and its volatile organic compounds degradation efficiency. *Nanomaterials (Basel)* 2023;**13**:1528. https://doi.org/10.3390/nano13091528
85. Elaouni A, El Ouardi M, Zbair M *et al.* ZIF-8 metal organic framework materials as a superb platform for the removal and photocatalytic degradation of organic pollutants: a review. *RSC Adv* 2022;**12**:31801–17. https://doi.org/10.1039/D2RA05717D
86. Hanif MA, Akter J, Kim YS *et al.* Highly efficient and sustainable ZnO/CuO/g-C3N4 photocatalyst for wastewater treatment under visible light through heterojunction development. *Catalysts* 2022;**12**:151. https://doi.org/10.3390/catal12020151
87. Kim DS, Han SJ, Kwak S-Y. Synthesis and photocatalytic activity of mesoporous TiO_2 with the surface area, crystallite size, and pore size. *J Colloid Interface Sci* 2007;**316**:85–91. https://doi.org/10.1016/j.jcis.2007.07.037
88. Kim DS, Kwak S-Y. The hydrothermal synthesis of mesoporous TiO_2 with high crystallinity, thermal stability, large surface area, and enhanced photocatalytic activity. *Appl Catal A Gen* 2007;**323**:110–8. https://doi.org/10.1016/j.apcata.2007.02.010
89. Wu Z, Fang B, Wang Z *et al.* MoS 2 nanosheets: a designed structure with high active site density for the hydrogen evolution reaction. *ACS Catal* 2013;**3**:2101–7. https://doi.org/10.1021/cs400384h

90. Chen H, Liang X, Liu Y *et al.* Active site engineering in porous electrocatalysts. *Adv Mater* 2020;**32**:2002435. https://doi.org/10.1002/adma.202002435
91. Koedsiri Y, Amornpitoksuk P, Randorn C *et al.* S-Schematic CuWO4/ZnO nanocomposite boosted photocatalytic degradation of organic dye pollutants. *Mater Sci Semicond Process* 2024;**177**:108385. https://doi.org/10.1016/j.mssp.2024.108385
92. Verma S, Tirumala Rao B, Singh R, Kaul R. Photocatalytic degradation kinetics of cationic and anionic dyes using Au–ZnO nanorods: role of pH for selective and simultaneous degradation of binary dye mixtures. *Ceram Int* 2021;**47**:34751–64. https://doi.org/10.1016/j.ceramint.2021.09.014
93. Wang Q, Qian X, Xu H *et al.* Enriched surface oxygen vacancies of Bi2WO6/NH2-MIL-68(In) Z-scheme heterojunction with boosted visible-light photocatalytic degradation for levofloxacin: performance, degradation pathway and mechanism insight. *Sep Purif Technol* 2023;**306**:122577. https://doi.org/10.1016/j.seppur.2022.122577
94. Zhou W, Jia J, Lu J *et al.* Recent developments of carbon-based electrocatalysts for hydrogen evolution reaction. *Nano Energy* 2016;**28**:29–43. https://doi.org/10.1016/j.nanoen.2016.08.027
95. Yang Z, Xia X, Shao L *et al.* Efficient photocatalytic degradation of tetracycline under visible light by Z-scheme Ag3PO4/mixed-valence MIL-88A(Fe) heterojunctions: mechanism insight, degradation pathways and DFT calculation. *Chem Eng J* 2021;**410**:128454. https://doi.org/10.1016/j.cej.2021.128454
96. El Ouardi M, Ait Layachi O, Amaterz E *et al.* Photo-electrochemical degradation of rhodamine B using electrodeposited Mn3(PO4)2.3H2O thin films. *J Photochem Photobiol A Chem* 2023;**444**:115011. https://doi.org/10.1016/j.jphotochem.2023.115011
97. Cai T, Zeng W, Liu Y *et al.* A promising inorganic-organic Z-scheme photocatalyst Ag3PO4/PDI supermolecule with enhanced photoactivity and photostability for environmental remediation. *Appl Catal B Environ* 2020;**263**:118327. https://doi.org/10.1016/j.apcatb.2019.118327
98. Jiang Z, Wan W, Li H *et al.* A hierarchical Z-scheme α-Fe 2 O 3/g-C 3 N 4 hybrid for enhanced photocatalytic CO2 reduction. *Adv Mater* 2018;**30**:1706108. https://doi.org/10.1002/adma.201706108
99. Liang Z, Cao Y, Qin H, Jia D. Low-heating solid-state chemical synthesis of monoclinic scheelite BiVO4 with different morphologies and their enhanced photocatalytic property under visible light. *Mater Res Bull* 2016;**84**:397–402. https://doi.org/10.1016/j.materresbull.2016.08.038
100. Wang D, Guo L, Zhen Y *et al.* AgBr quantum dots decorated mesoporous Bi2WO6 architectures with enhanced photocatalytic activities for methylene blue. *J Mater Chem A* 2014;**2**:11716–27. https://doi.org/10.1039/C4TA01444H
101. Nguyen TD, Bui QTP, Le TB *et al.* Co 2+ substituted for Bi 3+ in BiVO 4 and its enhanced photocatalytic activity under visible LED light irradiation. *RSC Adv* 2019;**9**:23526–34. https://doi.org/10.1039/C9RA04188E
102. Ge L. Novel Pd/BiVO4 composite photocatalysts for efficient degradation of methyl orange under visible light irradiation. *Mater Chem Phys* 2008;**107**:465–70. https://doi.org/10.1016/j.matchemphys.2007.08.016
103. Jiang H, Dai H, Meng X *et al.* Morphology-dependent photocatalytic performance of monoclinic BiVO4 for methyl orange degradation under visible-light irradiation. *Chinese J Catal* 2011;**32**:939–49. https://doi.org/10.1016/S1872-2067(10)60215-X
104. Wang M, Zheng H, Liu Q *et al.* High performance B doped BiVO4 photocatalyst with visible light response by citric acid complex method. *Spectrochim Acta A Mol Biomol Spectrosc* 2013;**114**:74–9. https://doi.org/10.1016/j.saa.2013.05.032
105. Xu X, Du M, Chen T *et al.* New insights into Ag-doped BiVO 4 microspheres as visible light photocatalysts. *RSC Adv* 2016;**6**:98788–96. https://doi.org/10.1039/C6RA20850A
106. Tang S, Wang Z, Zhang Y *et al.* Enhanced photocatalytic performance of BiVO4 for degradation of methylene blue under LED visible light irradiation assisted by peroxymonosulfate. *Int J Electrochem Sci* 2020;**15**:2470–80. https://doi.org/10.20964/2020.03.09
107. Kumar M, Vaish R. Photocatalytic dye degradation using BiVO 4 – paint composite coatings. *Mater Adv* 2022;**3**:5796–806. https://doi.org/10.1039/D2MA00316C

Oxford Open Materials Science, 2025, 5, 1–13
https://doi.org/10.1093/oxfmat/itaf005
Research article